

Revision 1: Word Count: 10540

# Structural Behavior of *C2/m* Tremolite to 40 GPa: A High-Pressure Single-Crystal X-ray Diffraction Study

Jason N. Ott<sup>1,3</sup>, Bora Kalkan<sup>1,2</sup>, Martin Kunz<sup>2</sup>, Genesis Berlanga<sup>1</sup>, Ali F. Yuvali<sup>1</sup>, and Quentin Williams<sup>1</sup>

<sup>1</sup>Department of Earth and Planetary Sciences, University of California, Santa Cruz, CA 95064, USA, <sup>2</sup>Advanced Light Source, Lawrence Berkeley National Lab, 1 Cyclotron Rd, Berkeley, CA 94720, USA, <sup>3</sup>Department of Earth and Space Sciences, Box 351310, University of Washington, Seattle, WA 98195, USA

## Abstract

The high-pressure structure and stability of the calcic amphibole tremolite ( $\text{Ca}_2\text{Mg}_5\text{Si}_8\text{O}_{22}(\text{OH})_2$ ) was investigated to  $\sim 40$  GPa at 300 K by single-crystal X-ray diffraction using synchrotron radiation. *C2/m* symmetry tremolite displays a broader metastability range than previously studied clinoamphiboles, exhibiting no first-order phase transition up to 40 GPa. Axial parameter ratios  $a/b$  and  $a/c$ , in conjunction with finite strain versus normalized pressure trends, indicate that changes in compressional behavior occur at pressures of  $\sim 5$  and  $\sim 20$  GPa. An analysis of the finite strain trends, using third-order Birch-Murnaghan equations of state, resulted in bulk moduli ( $K_{0T}$ ) of 72(7), 77(2), and 61(1) GPa for the compressional regimes from 0-5 GPa (regime I), 5-20 GPa (II), and above 20 GPa (III), respectively, and accompanying pressure-derivatives of the bulk moduli ( $K'_{0T}$ ) of 8.6(42), 6.0(3), and 10.0(2). The results are consistent with first-principle theoretical calculations of tremolite elasticity. The axial compressibility ratios of tremolite, determined as  $\beta_a : \beta_b : \beta_c = 2.22 : 1.0 : 0.78$  (regime I),

2.12:1.0:0.96 (II), and 1.03:1.0:0.75 (III), demonstrate a substantial reduction of the compressional anisotropy of tremolite at high pressures, which is a notable contrast with the increasingly anisotropic compressibility observed in the high-pressure polymorphs of the clinoamphibole grunerite. The shift in compression-regime at 5 GPa (I-II) transition is ascribed to stiffening along the crystallographic *a*-axis corresponding to closure of the vacant A-site in the structure, and a shift in the topology of the *a*-oriented surfaces of the structural I-beam from concave to convex. The II-III regime shift at 20 GPa corresponds to an increasing rate of compaction of the Ca-polyhedra and increased distortion of the Mg-octahedral sites, processes which dictate compaction in both high-pressure compression-regimes. Bond-valence analyses of the tremolite structure under pressure show dramatic overbonding of the Ca-cations (75% at 30 GPa), with significant Mg-cation overbonding as well (40%). These imply that tremolite's notable metastability range hinges on the calcium cation's bonding environment. The 8-fold coordinated Ca-polyhedron accommodates significant compaction under pressure, while the geometry of the Ca-O polyhedron becomes increasingly regular and inhibits the reorientation of the tetrahedral chains that generate phase transitions observed in other clinoamphiboles. Peak/background ratio of diffraction data collected above 40 GPa and our equation of state determination of bulk moduli and compressibilities of tremolite in regime III, in concert with the results of our previous Raman study, suggest that *C2/m* tremolite may be approaching the limit of its metastability above 40 GPa. Our results have relevance for both the metastable compaction of tremolite during impact events, and for possible metastable persistence of tremolite within cold subduction zones within the Earth.

## **Introduction:**

The physical and chemical processes that occur at subduction zones are central to understanding the dynamics of the crust and upper mantle of the Earth. The subduction of volatiles, such as the water contained in hydrated mineral phases, is responsible for much of the chemical cycling that occurs between the crust and upper mantle (e.g., Stern, 2002). The dewatering of such phases in the downgoing oceanic lithosphere and accreted sediments leads to flux melting in the overlying mantle wedge and the production of new continental crust through arc volcanism (Pawley and Holloway, 1993). Amphiboles are a complex group of hydrated silicate minerals with a wide range of chemical compositions that form under a wide range of pressures and temperatures (Hawthorne, 1981), and therefore are common constituents of altered oceanic crust and metamorphic rocks throughout subduction zones. While the thermodynamic stability of amphiboles has been experimentally constrained to ~2.5 GPa (depths of ~70-90 km) under equilibrium conditions in mid-ocean ridge basalt and andesitic bulk compositions (Poli and Schmidt, 1995; Schmidt and Poli, 1998; Poli and Schmidt, 2002), experimental work has demonstrated that mantle assemblages may potentially contain alkalic amphiboles stable at high temperatures to pressures beyond 12 GPa (e.g., Konzett and Fei, 2000). Moreover, extensive experimental work has shown that tremolite decomposition is heavily impeded by kinetic effects at ambient pressures, with tremolite persisting metastably for geologically-relevant times at temperatures outside of its stability field (Johnson and Fegley, 2000; 2003). Thus, amphiboles are known for their metastable persistence over long timeframes, and the motivations for this study include probing the structural properties of tremolite under metastable conditions. Indeed, several studies, including our recent spectroscopic study of the calcic amphibole mineral tremolite, suggest that the metastability of amphibole structures extends to much higher pressures than their formal thermodynamic stability range—to pressures as high as 50 GPa—in

lower-temperature/favorable chemical environments (Thompson et al., 2016; Yong et al., 2019; Ott and Williams, 2020; Bang et al., 2021). These observations are consistent with the apparent metastable persistence of tremolite to pressures of ~65 GPa under shock-loading (Simakov and Trunin, 1980). Hence, the potential abundance of tremolite within both a subset of large asteroids (Hamilton et al., 2021) and perhaps within the altered crusts of both Venus and Mars (Johnson and Fegley, 2003; Griffith and Shock, 1995) indicates that the behavior of shocked, metastable tremolite may be important for impact events on the terrestrial planets. Thus, a primary goal of this study is to illuminate the structural response of tremolite under large degrees of metastable compression.

The amphibole mineral tremolite ( $\text{Ca}_2\text{Mg}_5\text{Si}_8\text{O}_{22}(\text{OH})_2$ ) is an inosilicate with monoclinic symmetry that crystallizes in the crystallographic space group  $C2/m$  (Hawthorne, 1981). Figure 1 illustrates the general structure of tremolite and other monoclinic amphiboles—that of an interconnected network of I-beams composed of double-chains of corner-sharing  $\text{SiO}_4$  tetrahedra (T1 and T2 crystallographic sites) sandwiching sheets of octahedrally coordinated divalent Mg cations (M1, M2, and M3 sites) extending along the *c*-axis with  $\text{Ca}^{2+}$  cations (M4 sites) cross-linking the offset stacks of I-beams along the *b*-direction (Papike and Ross, 1970; Law and Whittaker, 1980). Adjacent I-beams along the *a*-direction are separated by the A site in amphiboles, which is vacant in the tremolite structure and is shown in Figure 1 as a void in the structure between the Ca cations along the *b*-axis.

The structure of tremolite has been studied previously at ambient conditions by X-ray and neutron diffraction (Hawthorne and Grundy, 1976), at low and high temperatures (Sueno et al., 1973; Yang and Evans 1996), and high-pressure X-ray structural refinements of tremolite were performed to a maximum pressure of 4.1 GPa by Comodi et al. (1991). The previous diffraction

studies of tremolite did not observe any pressure- or temperature-induced phase transitions. However, phase transitions have been found in other monoclinic amphiboles at elevated pressures and temperatures. In the cummingtonite-grunerite solid solution series ((Mg,Fe)<sub>2</sub>(Mg,Fe)<sub>5</sub>Si<sub>8</sub>O<sub>22</sub>(OH)<sub>2</sub>), pressure-induced phase transitions have been observed from the *C2/m* to *P2<sub>1</sub>/m* space groups at ~1.21 GPa for cummingtonite (Yang et al., 1998) and ~3 GPa for grunerite (Yang et al., 1998; Boffa Ballaran et al., 2000; Yong et al., 2019). A second phase transition was reported for grunerite from the *P2<sub>1</sub>/m* to *C2/m* space groups at ~19.2 GPa (Yong et al., 2019). A temperature-induced transition in cummingtonite has been observed from the *P2<sub>1</sub>/m* to the *C2/m* space group in the 240 K to 373 K range, depending upon its composition and cation site occupancies (Prewitt et al., 1970; Sueno et al., 1972; Yang and Smyth, 1996). The structural similarity (e.g., vacant A-site) between the cummingtonite-grunerite solid solution and tremolite suggests the possibility that similar phase transitions might occur in tremolite. Our Raman spectroscopic study of tremolite to 49 GPa showed indications of possible shifts in compressional mechanisms at pressures above 10 GPa, but the structural origin of these shifts is unknown (Ott and Williams, 2020).

In this study, we perform single-crystal X-ray diffraction experiments with synchrotron radiation to investigate the compressibility and metastability of tremolite to ~40 GPa. We refine the structure of tremolite under ambient conditions and high pressures at quasi-hydrostatic conditions. The results of the structural refinements are used to determine the unit cell parameters and volume of the tremolite structure under compression and analyze the elastic response of the mineral. Our objectives are to determine whether tremolite undergoes any subtle phase transitions or changes in its compressional mechanisms during compaction, and to

compare the high-pressure behavior of tremolite to that of other monoclinic amphiboles under pressures relevant to the crust and upper mantle in subduction zones.

### **Experimental Methods:**

The tremolite used in this study is a natural sample from the Crevoladossola marble of the Novara province of Italy with composition  $\text{Na}_{0.10(2)}\text{K}_{0.01(2)}\text{Ca}_{2.06(17)}\text{Mg}_{4.93(10)}\text{Al}_{0.13(1)}\text{Si}_{7.88(24)}\text{O}_{22}(\text{OH}_{0.98(29)}\text{F}_{1.02(14)})$  as determined by energy-dispersive X-ray spectroscopy (EDS) using a ThermoFisher Scientific Apreo variable-pressure scanning electron microscope (SEM) at 20kV accelerating voltage. The composition was determined through analysis of 5 regions of a polycrystalline tremolite sample with a polished face of dimensions  $\sim 5 \times 15$  mm normalized to an oxygen and fluorine content of 24 apfu (Hawthorne and Oberti, 2007). The results of this EDS analysis are included in supplemental data table S1. We performed a Raman spectroscopic study of crystals from the same bulk sample previously, and there were no indications of calcite or dolomite inclusions in the mineral. There is also no evidence of significant substitution of  $\text{Fe}^{2+}$  for  $\text{Mg}^{2+}$  in the M1, M2, or M3 octahedral sites, and therefore the mineral appears to be of nearly end-member composition (Ott and Williams, 2020).

Ambient and high-pressure single-crystal X-ray diffraction studies were carried out at beamline 12.2.2 at the Advanced Light Source (ALS), Lawrence Berkeley National Laboratory (Kunz et al., 2005). Elongated crystals from the tremolite hand sample were crushed in an agate mortar and pestle, and several block-shaped single-crystals with no visible fractures were selected for this study.

### *Ambient Conditions X-ray Diffraction:*

An irregularly shaped tremolite single-crystal was selected under a polarized microscope using a micromesh mount (Mitegen USA) with 30  $\mu\text{m}$  aperture size and was mounted on the goniometer of the STOE StadiVari X-ray single-crystal diffractometer at end-station 1 of beamline 12.2.2. The diffraction data were collected with an RDI CMOS 1M detector. Shutterless single-crystal X-ray diffraction measurements were performed using synchrotron radiation monochromated by silicon (111) at an energy of 30 keV (0.4133  $\text{\AA}$ ). Data collection ( $\phi$ -scans) was performed at room temperature at step widths of  $1^\circ$  using an x-ray beam focused to  $\sim 80(\text{H}) \mu\text{m} \times 50(\text{V}) \mu\text{m}$  in FWHM. A typical exposure time of 0.5-2 s/ $^\circ$  that maximizes the intensities of the diffraction peaks without saturation was selected. A NIST standard (SRM 1990, single-crystal ruby sphere) was used to calibrate the beamline characteristics, such as sample distance and wavelength (Wong-Ng et al., 2001). Data were integrated using XAREA 1.76 (Stoe and Cie, 2009). Integrated intensities were scaled and corrected for absorption (with the numerical absorption correction) using LANA (Koziskova et al., 2016) and X-RED32 (equivalent to the work of Coppens (1970)) packages embedded in XAREA.

### *High-Pressure X-ray Diffraction:*

High-pressure diffraction data were collected using tremolite single-crystals of dimensions  $\sim 10 \times 20 \times 20 \mu\text{m}$  loaded into either a BX-90 diamond anvil cell (DAC) equipped with 350  $\mu\text{m}$  culet type Ia diamond anvils, or a short symmetric-type DAC equipped with 300  $\mu\text{m}$  culet  $80^\circ$  aperture Boehler-Almax type diamonds. The gaskets were machined by pre-indenting 250  $\mu\text{m}$  thick rhenium to 30  $\mu\text{m}$  thickness, and a circular 130  $\mu\text{m}$  diameter sample chamber was drilled with a laser-milling system. Residue from the laser milling process was

removed by hand initially, and then gaskets were cleaned ultrasonically with acetone followed by deionized water. Gaskets were mounted to the piston-side diamond anvil, and the tremolite crystals loaded at the center of the sample chamber and several small ruby crystals (< 10  $\mu\text{m}$  diameter) placed around the sample as a pressure standard. The DAC was gas-loaded at the ALS with neon as a pressure transmitting medium, as this medium has been shown to behave close-to-hydrostatically up to pressures approaching 50 GPa (Klotz et al., 2009). Diffraction data were collected up to  $\sim 47$  GPa over pressure-steps ranging from 0.5 to 5 GPa. After sample equilibration for 15 minutes at each pressure-step, pressure measurements were made using ruby fluorescence in conjunction with the R1 and R2 peak locations (Mao et al., 1986). Pressure measurements were repeated after collection of each set of diffraction images to monitor for any drift in pressure, with no detected changes in pressure larger than the uncertainty of the calibration of Mao et al (1986).

The high-pressure diffraction data were collected at end-station 2 of beamline 12.2.2 using synchrotron X-rays monochromated by silicon (111) with an energy of 30 keV (wavelength of 0.4132(1)  $\text{\AA}$ ) that was focused to a 10 x 10  $\mu\text{m}$  spot. The diffracted X-rays were collected on a Pilatus3 S 1M fast detector. A typical exposure time of 1.0 s/ $^\circ$  was selected for data collection. Detector distance and wavelength calibration were performed using a NIST single-crystal ruby sphere (Wong-Ng et al., 2001). The sample was aligned to the rotational center of the goniometer, and data were collected throughout the angular range of  $\theta = -30^\circ$  to  $30^\circ$  (in 0.50 $^\circ$  and 1.00 $^\circ$  increments) for a total coverage of 60 $^\circ$  sample rotation.

Data collection was performed using a LabView code produced at the ALS, and data were reduced to hkl-sorted structure factors using APEX3 (Bruker, 2016). Unit cell parameters at each pressure-step were determined up to 38.7 GPa by a least-squares refinement of  $\sim 300$

reflections harvested from 60-120 frames in the  $\theta = -30^\circ$  to  $+30^\circ$  range. After indexing of the diffraction pattern and determination of the Bravais lattice, the NIST ruby calibration was applied, and the unit cell parameters were refined. Loss of intensity in the diffraction data collected at pressures above 38.7 GPa resulted in a weak peak/background ratio in the reciprocal lattice that prevented indexing and refinement of the unit cell parameters. The data were integrated using the program SAINT v8.34A. A few individual reflections (with negative and almost zero intensities) were removed from the data set because their intensities were affected by simultaneous diffraction events in the diamond anvils. Data were corrected for the reduction of reflection intensities due to the DAC-gasket shadowing in APEX. Structures were solved using direct methods in SHELXS and further refinements were carried out with SHELXL (Sheldrick, 2008) by full-matrix least-squares on  $F^2$ . A total of  $\sim 250$  unique reflections were available for subsequent structural analysis.

The crystal structures were refined at 7 pressure points (set 3, in the range of 0-30 GPa, supplemental table S2) with isotropic displacement parameters. For every structure,  $\sim 42$  parameters including overall scale factor, isotropic atomic displacement factors, and fractional coordinates of the atoms were refined. Substitutional disorder between oxygen and fluorine was modeled in the ambient-conditions diffraction data by constraining O3 and F anions to share the same atomic position and displacement parameters and refining their partial occupancy of the O3 site. The resultant O/F occupancy ratio of 0.56/0.44 lies within the margin of uncertainty of the EDS compositional analysis, therefore the occupancy of the O3 site was fixed at these values for all high-pressure structural refinements.

## Results and Discussion:

### *Ambient Pressure Structural Refinement and Unit Cell Parameters:*

Analysis of the ambient pressure single-crystal data produced a structural model for tremolite with unit cell parameters  $a = 9.833(2) \text{ \AA}$ ,  $b = 18.046(4) \text{ \AA}$ ,  $c = 5.274(1) \text{ \AA}$ ,  $\beta = 104.76(3)^\circ$ , and  $V = 904.9(3) \text{ \AA}^3$  and systematic absences consistent with the  $C2/m$  space group. The atomic positions of the ambient pressure structural refinement are presented in Table 1 and Figure 1 shows the refined structure. This result is in excellent agreement with previous work on near end-member-composition tremolite at ambient conditions (e.g., Comodi et al., 1991; Yang and Evans, 1996). In particular, the  $\beta$ -angle, which is sensitive to small amounts of cummingtonite substitution (Yang and Evans, 1996), is indistinguishable from those of tremolites with negligible substitution. Atomic positions from our ambient pressure structural refinement were used to calculate the thickness and separation of the I-beam structural unit. In the following discussion, we use same the nomenclature as Comodi et al. (1991) to refer to the thickness of the I-beam in the  $a$ -direction between geometrically equivalent oxygens with a single-prime (e.g., O4-O4'), and separation between I-beams with a double-prime (e.g., O4-O4''). Our measured thickness of  $6.591(3) \text{ \AA}$  at the center of the I-beam (O7-O7' distance) and  $7.054(3) \text{ \AA}$  at the edge (O4-O4' distance) are respectively 2.6 and 1.4% larger than the room-pressure results of Comodi et al. (1991), which may be ascribed to compositional differences in our respective tremolite samples. Still, we find a similar value for the reduction in thickness at the center of the I-beam ( $\sim 0.5 \text{ \AA}$ ) attributable to the bowed structure of the  $\text{SiO}_4$  double-chains in amphiboles as reported in previous studies (e.g., Papike and Clark, 1968; Comodi et al., 1991). The hydrogen atoms were not resolvable in the electron density map and, therefore, were not included in the refinement of the tremolite structure.

### *High Pressure Unit Cell Parameters and Perseverance of C2/m Structure:*

Results for the unit cell parameters and volume of the tremolite structure for the ambient- and high-pressure experiments are presented in Table 2, and the normalized change in the volume and unit cell parameters are shown up to 38.7 GPa in Figure 2. Tremolite persists in the C2/m space group throughout the pressure range investigated, with no apparent discontinuities in the volume or axial parameters, and thus no indication that tremolite undergoes a first-order phase transition over the pressure range of this study, in accord with our prior Raman results (Ott and Williams, 2020).

The evolution of the monoclinic  $\beta$ -angle in tremolite over the pressure range of the experiment is, however, complex. Figure 3 shows the change in the  $\beta$ -angle as a function of pressure, which initially increases, as in other monoclinic amphiboles investigated by high-pressure single-crystal XRD studies (Comodi et al., 1991; Yang et al., 1998; Yong et al., 2019). However, in tremolite, the  $\beta$ -angle reaches a maximum between 10 and 13 GPa and begins decreasing, until ~22-28 GPa, where the trend reverses, and the  $\beta$ -angle appears to weakly increase in the data set (set 2) that accesses this pressure-range. As the data collected above 38.7 GPa could not be indexed, it is unclear whether the decrease in the  $\beta$ -angle at the maximum pressure datum represents another change in the trajectory of the  $\beta$ -angle or scatter/uncertainty in the data. Although the behavior of the monoclinic angle with pressure is clearly complex, its total variation is quite small: its maximum change (near 12 GPa) is substantially less than a degree.

Whittaker (1960) ties the M4-O4 bond length and thus the radius of the ion occupying the M4 site to the  $\beta$ -angle of monoclinic amphiboles, which in turn can be related to the degree of closest packing of the oxygen anions in the structure (Yong et al., 2019). In the X-ray diffraction

studies by Yang et al. (1998) on cummingtonite and Yong et al. (2019) on grunerite, the M4 site is primarily occupied by  $\text{Fe}^{2+}$  cations and the initial  $\beta$ -angle of  $\sim 102^\circ$  increases through the entire pressure range of their experiments. Yang et al. (1998) and Yong et al. (2019) observe that during the  $C2/m$ - $P2_1/m$  phase transition the  $\text{SiO}_4$  double chain splits into two distinct chains: an O-rotated B-chain corresponding to the sense of rotation of both chains in the  $C2/m$  structure, and an S-rotated A-chain. Papike and Ross (1970) provide a discussion of chain rotation in inosilicates. This reduction in symmetry of the structure is accompanied by an increase in the coordination of the M4 sites in cummingtonite and grunerite from six—two M4-O2 bonds, two M4-O4 bonds, and two M4-O6 bonds—to seven by the inclusion of one M4-O5 bond in the coordination of the M4 site. The  $P2_1/m$ - $C2/m$  phase transition to  $\gamma$ -grunerite at  $\sim 19$  GPa described by Yang et al. (2019) involves a return of both tetrahedral chains to an O-rotated configuration in conjunction with a discontinuous increase in the  $\beta$ -angle to  $107.99^\circ$  and a return of the M4 site to six-fold coordination—with the difference that the M4 site is now coordinated to two O5 anions in place of the two O6 anions in the low-pressure  $C2/m$  phase. Therefore, the sequence of increasing-pressure phase transitions in the cummingtonite-grunerite solid solution allows the oxygen anions to move into more closely packed configurations with higher pressures. In contrast, the M4 site of tremolite, with its larger, eight-fold coordinated  $\text{Ca}^{2+}$  cations, generates a larger ambient pressure  $\beta$ -angle, implying that the oxygen anions are more closely packed than in the cummingtonite-grunerite solid solution series at low pressures. Indeed, the ambient-pressure volume of tremolite is  $\sim 1\%$  less than that of grunerite (Yong et al., 2019). The increase of the  $\beta$ -angle to a maximum at pressures of  $\sim 11$ - $14$  GPa, followed by a decreasing trend that reverses to weakly increase at pressures greater than 22 GPa, suggests that the structural accommodation of compression in tremolite is governed by steric effects created by

the presence of the more sizeable calcium cation in the M4 site of tremolite and its coordination to eight oxygen anions throughout its compaction. The high-pressure shifts in the trend of the  $\beta$ -angle may also be driven by the significant changes in the geometry of the M4 site under compression. As shown in Figure 6, the M4-O5 bond distance in tremolite is by far the most compressible, with it initially being the longest bond distance associated with the Ca-polyhedra and becoming smaller than the M4-O6 distance at pressures near 16 GPa. The close approach of the M4-O5 distance to the M4-O6 distance occurs near the pressure at which the  $\beta$ -angle reaches its maximum: this is in accord with the observation by Sueno et al. (1973) that the shift in 6- to 8-fold coordination of the M4 cation results in a general increase in the  $\beta$ -angle: this is a transition that we clearly document under compression. The mean size of the M4 site also clearly is seminal here: it has long been recognized that decreases in the M4 site size produce an increase in the  $\beta$ -angle at ambient pressure (e.g., Whittaker, 1960). At higher pressures, the topological requirement that the tetrahedral double chains remain in register with the octahedral strips in the structure (through the M4 site) dictate that the sizes and distortions of the M1, M2, and M3 sites must also play a role in the ultimate value of the  $\beta$ -angle: a conclusion consistent with Hawthorne and Oberti's (2007) analysis of the factors governing the  $\beta$ -angle. Thus, the most likely interpretation of the decrease in the  $\beta$ -angle above 11-14 GPa is that it is generated by topological constraints generated by the relative compressibilities of the M1, M2, and M3 sites (which, as illustrated in Figure 6, are notably smaller than that of the M4 site), and hence that the (meta)stability of the tremolite structure dictates that the incompressibility of the octahedral strip begins to dictate the pressure dependence of the  $\beta$ -angle above  $\sim$ 14 GPa.

*Bulk Moduli, Equations of State, and Axial Compressibilities:*

While our analysis shows that tremolite does not undergo a phase transition up to 39 GPa, there are, nonetheless, slope changes in the trends of the axial parameters and the volume of the tremolite unit cell with increasing pressure (Figure 4). These slope changes are clearly apparent in the variations of the axial ratios of the unit cell with pressure; these are most readily fit by linear trends across three different pressure intervals. Figure 4 also illustrates the axial ratios  $a/b$  and  $a/c$  for tremolite alongside the ratios reported for cummingtonite (Yang et al., 1998) and grunerite (Yong et al., 2019). The reported results of Yang et al. (1998) display a change in the slopes of  $a/b$  and  $a/c$  that occurs in conjunction with the  $C2/m-P2_1/m$  phase transition in cummingtonite. Interestingly, in the results of Yong et al. (2019), the axial ratios for grunerite show both slope changes and discontinuities that occur with the  $C2/m-P2_1/m$  transition near  $\sim 7$  GPa and the  $P2_1/m-C2/m$  transition near  $\sim 19$  GPa. Both the studies of cummingtonite and grunerite conclude that changes in compression mechanisms occur in conjunction with the observed phase transitions. The changes in the pressure dependences of the axial ratios of tremolite suggest that the structure undergoes isostructural shifts in its compressional mechanisms, with the first change being near  $\sim 5$  GPa and a second near  $\sim 20$  GPa. These shifts are likely not abrupt and could span a range of roughly  $\pm 1$  GPa for the lower pressure transition, and a more loose bound of  $\pm 2$  GPa for the higher-pressure shift. Interestingly, the apparent changes in the compression mechanism of tremolite occur at close to the same pressures as the phase transitions and compressibility changes observed in grunerite.

Whether these shifts in the pressure dependences of axial ratios are manifested in the bulk elasticity of tremolite can be assessed from equation of state fits to the different compressional ranges of Figure 4. In fitting the pressure and volume data to an equation of state, data were

transformed and plotted on an  $F_E$ - $f_E$  plot, where  $f_E$  was calculated using the Eulerian definition of finite strain as

$$f_E = \frac{1}{2} \left[ \left( \frac{V_0}{V} \right)^{\frac{2}{3}} - 1 \right] \quad (1)$$

and  $F_E$  is the normalized pressure determined as

$$F_E = \frac{P}{3f_E(1+2f_E)^{\frac{5}{2}}} \quad (2)$$

using the methodology described by Birch (1978). The  $F_E$ - $f_E$  results for our tremolite data are shown in Figure 5a, and these also suggest that there are three separate regimes of compressional behavior (we refer to these, with increasing pressure, as tremolite compression-regimes I, II, and III). The slope changes occur at finite strains corresponding to ~5 GPa and ~20 GPa, which are consistent with the changes in the slopes of the axial ratios of tremolite (Figure 4). Any relationship with the changes in the  $\beta$ -angle is less clear, but the higher-pressure shift may be associated with a change in the pressure-dependence of this angle. Least-square fits to the  $F_E$ - $f_E$  data display linear trends with varying positive slopes in each regime (with the highest-pressure regime having the *steepest* positive slope), thus indicating that the data are best described using a sequence of third-order equations of state (Angel, 2000b). The values of  $K_0$  and  $K'$  are estimated by applying the equations:

$$F_E = K_0(1 + a f) \quad (3)$$

with  $K_0$  determined as the intercept of the fit line with the  $F_E$ -axis (Figure 5a), and

$$K' = \frac{2}{3}a + 4 \quad (4)$$

for data fit by a third-order equation of state (Birch, 1978; Angel, 2000b), in which  $K_0$  is the intercept of the  $F_E$ - $f_E$  trend, and  $a$  is the slope. Data in compression-regime I were also fit using a constrained isothermal bulk modulus of 78 GPa as determined for tremolite by Brown and

Abramson (2016) using Reuss bounds and elastic moduli measured by impulsive stimulated light scattering. The volume and pressure data for each compression-regime were used along with our estimated values for  $K_0$  and  $K'$  to fit third-order Birch-Murnaghan equations of state with the program EosFit7 (Gonzalez Platas et al., 2016), and the results are shown in Figure 5b and Table 3. Our unconstrained third-order fit of the equation of state of tremolite in compression-regime I results in a significantly lower value of  $K_0$  (72 ( $\pm 7$ ) GPa) than the value of 85 GPa reported by Comodi et al. (1991). The disagreement can be attributed to our use of a third-order finite strain equation of state relative to their linear fit of pressure-volume data (which implicitly assumes a  $K'$  of 0). The value of  $K_0$  of tremolite was reanalyzed by Comodi et al. (2010) using a second-order equation of state (an assumed  $K'$  of 4) using the Comodi et al. (1991) data, resulting in a  $K_0$  of 76 ( $\pm 3$ ). The values of  $K'$  that we generate (8.6 ( $\pm 4.2$ ) for our unconstrained third-order fit, and 5.7 ( $\pm 2.1$ ) for the fit with the bulk modulus constrained) would bring these values into better agreement. Values of  $K'$  that are greater than 4 for tremolite are also indicated by first-principles calculations (Peng and Mookherjee, 2020): these yield, with the local density approximation (LDA), a bulk modulus of 78.5 GPa, a  $K'$  of 5.2, and a zero-pressure volume underestimated by 2%.

A novel feature of our results is that the  $K'$  values of compression-regimes II and III are each high as well, with a notably large value of  $K'$  (10.0) in the highest-pressure regime; and the zero-pressure intercept of the trend of regime III (corresponding to  $K_0$ ) is substantially below that of the ambient bulk modulus of tremolite. These results are indicative of a positive value of  $K''$ , which is a quite unusual result for a crystalline silicate—almost all silicates for which the second derivative of the bulk modulus has been constrained have negative values for this parameter (e.g., Bass, 1995), and the default  $K''$  value within the 3rd order Birch-Murnaghan equation of

state is also negative for normal  $K'$  values (Birch, 1978). Indeed, the 4th order fit shown in Figure 5d illustrates this anomalous result: the upward curvature demonstrates that a positive  $K''$  is required for tremolite. This unusual value for  $K''$  provides an additional motivation for the division of the data into multiple compressional regimes. The positive value of  $K''$  produces progressively larger values of  $K'$  across each of the three compressional ranges that we identify based on our structural observations, and that occur as distinct domains within the  $F_E$ - $f_E$  plot.

The question that arises is thus: why does the inferred  $K_0$  drop and  $K'$  increase within our highest-pressure range (or, why is  $K''$  positive)? In this regard, the first-principles simulations of tremolite to 10.6 GPa of Peng and Mookherjee (2020) provide some insights: within their LDA simulations, the shear elastic constant  $c_{66}$  has a negative pressure-derivative at all pressures, and  $c_{44}$  is likely to have a negative derivative above  $\sim 12$  GPa. A quadratic extrapolation of their results on  $c_{13}$  and  $c_{22}$  (in their simulations, the largest elastic constant) indicates that both this off-diagonal modulus and principal modulus may begin softening near 32 and 36 GPa, respectively—well within the pressure-range of our results. This extrapolation is relatively long in pressure from Peng and Mookherjee's (2020) results, and the precise onset pressure of a negative derivative of these moduli (each of which contributes to the bulk modulus) is uncertain: lower pressures of onset are by no means precluded. Hence, the available calculations on the elasticity of tremolite under pressure strongly suggest that a suite of its elastic constants have negative slopes at high pressures. As such, although we obviously do not have constraints on the pressure dependence of tremolite's full elastic tensor through the pressure range of our experiments, available indications are that there will be an admixture of both hardening and softening elastic constants at high pressures. The onset of softening of multiple constants could give rise to a lower inferred  $K_0$  from our highest-pressure compressional range; the effect on  $K'$

and  $K''$  of individual elastic constants with negative pressure-shifts is less straightforward to predict, but will hinge on the net pressure-dependences of both the primary and off-diagonal constants that contribute to the bulk modulus. A key finding here is that the strongly non-linear pressure dependences of a range of tremolite's elastic constants generated by theory (Peng and Mookherjee, 2020) are likely to impact the higher-pressure, metastable compaction of tremolite: a result compatible with our observation of differing compressional regimes, and positive  $K''$  values, within this material.

Tremolite compresses anisotropically over the pressure range explored in the experiment, with the greatest reduction of unit cell length occurring along the  $a$ -axis ( $\sim 11\%$  reduction at 38.7 GPa), followed by the  $b$ -axis ( $\sim 7\%$  reduction), and the least compressible direction along the  $c$ -axis ( $\sim 5\%$  reduction). The axial compressibilities of tremolite, defined by Angel (2000a) as  $\beta_{10} = \frac{1}{(3K_{10})}$ , were calculated using the program EosFit7 (Gonzalez Platas et al., 2016) to fit the third-order Birch-Murnaghan equation of state to the unit cell parameter data for each compression-regime (Table 3). Tremolite's initial linear compressibilities  $\beta_a$ ,  $\beta_b$ , and  $\beta_c$  are calculated as 0.0082(4), 0.0037(19), and 0.0029(2) GPa<sup>-1</sup>, respectively. Our results for  $\beta_b$  and  $\beta_c$  agree within the estimated standard deviations with the values of  $\beta_b = 0.0027$  GPa<sup>-1</sup> and  $\beta_c = 0.0026$  GPa<sup>-1</sup> reported by Comodi et al. (1991), while our larger result of  $\beta_a = 0.0082$  GPa<sup>-1</sup> (reported as 0.0059 GPa<sup>-1</sup> by Comodi et al., 1991) again appears to stem from the difference between a linear pressure-axial length fit as opposed to our usage of a third-order equation of state, which allows for refinement of the pressure-derivative of the compressibility. Both our results and those of Comodi et al. (1991) differ from the first-principles theory in the relative order of the axial compressibilities: Peng and Mookherjee (2020) predict that  $\beta_a > \beta_c > \beta_b$ , while the experiments each have  $\beta_a > \beta_b > \beta_c$ . The origin of this discrepancy is unclear, but the

compressibilities along the *b*- and *c*-directions are substantially closer to one another in the experiments than in the theory: this similarity is also in accord with elastic measurements on tremolite (Brown and Abramson, 2016).

The order of axial compressibilities also differs between tremolite and the amphiboles of the cummingtonite-grunerite solid solution. In our analysis of tremolite, we calculate the initial axial compression-ratio ( $\beta_a : \beta_b : \beta_c$ ) as 2.22:1.0:0.78 (in comparison to Comodi et al.'s (1991) ratio of 2.19:1.00:0.96), while Yang et al. (1988) reported 2.83:1.00:1.17 for the low-pressure *C2/m* phase of cummingtonite and Yong et al. (2019) calculated a ratio of 1.49:1.00:1.10 for *C2/m*  $\alpha$ -grunerite. All three minerals are highly anisotropic under compaction, with the *a*-axis being the most compressible direction. However, for tremolite, the *c*-axis is the least compressible direction, while for cummingtonite and grunerite, it is the *b*-axis. Since the changes in the compressibility for grunerite occur with phase transitions at similar pressures to the compressibility changes in tremolite, it is interesting to contrast the behavior of the two minerals across the three compression-regimes we observe in tremolite, and the transitions in grunerite. With each change in the compression mechanism of tremolite, the compressibilities along the *a*- and *c*-axes are reduced, while along the *b*-axis, the compressibility fluctuates near  $\sim 0.0030 \text{ GPa}^{-1}$  (Table 3) across all three regimes, leading to a general reduction in the compressional anisotropy of tremolite with each regime change. In contrast, as grunerite transitions from *C2/m*  $\alpha$ -grunerite  $\rightarrow P2_1/m$   $\beta$ -grunerite  $\rightarrow C2/m$   $\gamma$ -grunerite, the ratios  $\beta_a : \beta_b : \beta_c$  evolve from 1.49:1.0:1.1  $\rightarrow$  1.86:1.0:0.99  $\rightarrow$  0.56:1.00:1.41 with the compressibility along the *b*-axis again fluctuating in a narrow range, and increasingly anisotropic compressibilities along the other crystallographic axes (Yong et al., 2019). Hence, the compressional anisotropy of tremolite is substantially decreased by pressure, with the relative ratios of axial compressibilities being 1.03:1.0:0.75 in

the highest-pressure compressional range. A decrease in anisotropy of tremolite under compression is also observed in the theoretical results (Peng and Mookherjee, 2020), but the evolution towards nearly equal compressibilities of the  $a$  and  $b$  axes that we observe involves a substantially more isotropic compressibility than is predicted theoretically. In contrast, the compressional anisotropy of grunerite is augmented by its sequence of transitions. Thus, the substantial stiffening of the  $a$ -axis in tremolite under compression implies that the vacant A-site and the octahedral layers become substantially less compressible at the highest pressures of this study.

#### *High-pressure Structure Refinement and Compression Mechanisms:*

High-pressure structural refinements were conducted for multiple pressures in each compression-regime: at ambient pressure and 4.2 GPa in regime I, 9.6, 13.1, and 16.8 GPa in regime II, and 23.6 and 29.2 GPa in compression-regime III (supplemental table S2). Isotropic refinement details are presented in the supplemental tables (S2, S3). We conducted an analysis of changes in the bond lengths (Figure 6) and polyhedral/structural units (Figure 7) of the tremolite structure, generated by the structure refinements, to evaluate its accommodation of compaction in each compression-regime. The compression mechanism of tremolite has been previously characterized to 4.1 GPa in the work of Comodi et al. (1991) and consists largely of a flattening of the bowed tetrahedral chains such that the I-beam structural unit takes on a more uniform thickness in the  $b$ -crystallographic direction and, consequently, the volume of the vacant A-site is reduced. Comodi et al. (1991) also note that compaction along the less compressible  $b$ - and  $c$ -axes is primarily accommodated by an increased sense of O-rotation in the SiO<sub>4</sub> tetrahedral double-chains and distortion of the M site polyhedra. Our experimental results are concordant

with this prior work and demonstrate that these trends continue with increasing pressure until, at the compression-regime I-II transition, the tetrahedral chains are flattened, and the I-beam displays a uniform thickness (Figure 7c). This crossover of the O4-O4' distance (at the edge of the I-beams) and the O7-O7' distance (at the center of the I-beams) near 6 GPa (Figure 7c) is also observed in the LDA simulations at somewhat higher pressures (~8-9 GPa), but not in the pressure range of simulations using the Generalized Gradient Approximation (GGA) (Peng and Mookherjee, 2020). By the same token, the O4-O4'' and O7-O7'' distances (corresponding to the I-beam spacing at their edge and center, respectively) also cross-over near this pressure. Accordingly, we attribute the marked stiffening of (particularly) the *a*-axis of tremolite at the transition from compression-regime I to II to the elimination of bowing of the I-beams (and, correspondingly, the onset of a flattened space between them). Thus, we attribute the shift in the ratios of axial compressibilities (Figure 4) to the loss of concavity of the I-beams, and the onset of convexity.

The shift in compression from regime II to III appears to be more complex. The most compressible unit within the structure is the Ca-site, and its compressibility appears to be augmented within regime III (Figure 7b). Its internal geometry shifts markedly (Figure 6f): the two initially longest calcium-oxygen ions (O5) compact dramatically under compression, and crossover with the two Ca-O6 distances near the onset of regime III. As such, the eight-fold Ca ion environment becomes substantially more regular under compression. In the same pressure-range, a number of the Mg-O distances associated with particularly the Mg2 and Mg3 sites appear to undergo increases in their compaction rate, as well (Figures 6b,c), as do their polyhedral volumes (Figure 7c). Furthermore, the overall variability in bond distances in both the Mg1 and Mg3 sites is clearly enhanced in regime III, implying greater distortion of the Mg-sites.

For comparison, few clear changes are observed in the bond angles associated with the tetrahedral chains (Figure 7a) across the II-III shift. Accordingly, regime III appears to be characterized by regular (but rapid) contraction of the Ca-polyhedron, accompanied by greater compaction and distortion of the Mg-octahedra (the space between I-beams—the vacant A-site—does continue to contract, bowing inward with its center becoming narrower than its edge: Figure 7c). In effect, compaction in regime III appears modulated by internal deformation and compression of the M sites.

The compressional mechanisms acting in regimes II and III are consistent with the presence and increased regularity of the eight-fold coordinated calcium cations in the M4 site being critical in the inhibition of transitions into more closely packed structures. This importance of the M4 site in the compressional behavior of tremolite is supported by the results of our previous Raman spectroscopic study of tremolite to ~50 GPa, in which shifts in intensities of spectral features above 10 GPa within low-frequency spectral regions associated with cation-oxygen displacements are likely to be indicative of changes in the bonding environment of the M4 site, but with no indication that tremolite undergoes a phase transition (Ott and Williams, 2020).

The role of differing cations (and particularly Ca) in the structural metastability of tremolite under pressure can be quantitatively assessed from a bond-valence analysis (Brown, 2002). In these calculations, the steric stress on the structure is evaluated from the deviation of the bond-valence sum for each cation from the ideal value ( $\Sigma(S_{ij}) - v_i/v_i$ ), where  $S_{ij}$  is the bond-valence between atoms  $i$  and  $j$ , and  $v_i$  is the absolute value of atom  $i$ 's valence for each cation. Figure 8 shows the results on the overbonding of the different cations in tremolite as pressure is increased (here, negative values would imply underbonding; positive values indicate

overbonding). At ambient pressures, the cations within tremolite are notably close to zero overbonding (or underbonding)—each cation within the structure appears to be nearly optimally bonded, indicating a sterically very compatible structure. At high pressures, the calcium ion progressively becomes the most overbonded cation, with an overbonding level of ~75% at 30 GPa. The magnesium octahedra also become overbonded (and overbonded at similar levels to one another) under compression, but only at the ~40% level. Hence, with such large degrees of overbonding of the Ca-ion in tremolite, the issue of how and why tremolite remains metastable to pressures of 40-50 GPa at 300 K emerges. The explanation appears likely to be topological: under pressure, the Ca-ion's environment converges on a not-overly distorted 8-fold site, held between comparatively rigid structural I-beams within the tremolite structure. And, by the same token, the ability of the tetrahedral chains to reorient also hinges on a marked and discontinuous disruption of the Ca-polyhedron.

### **Implications:**

Structural similarities between single- and double-chain inosilicates naturally lead to comparisons of the structural properties and phase transition behavior of the pyroxene and amphibole structures. The sensitivity of phase transitions to M site cation size and shifts in M site coordination through a sequence of  $C2/c$ - $P2_1/c$ - $C2/c$  phase transitions in high-pressure studies of both natural and synthetic clinopyroxenes has been previously noted (e.g., Arlt et al., 1998; Arlt and Angel, 2000; Yang and Prewitt, 2000; Tribaudino et al., 2001), although high-pressure structural studies of the clinoamphiboles have been limited. The cummingtonite-grunerite solid solution series undergoes a series of potentially analogous phase transitions at 300

K in clinoamphiboles under compression, but the preservation of the  $C2/m$  phase of tremolite to pressures of 40 GPa and higher raises questions of the role that calcium plays in dictating the high-pressure metastability of tremolite. A plausible explanation for this difference in behavior is that the size and occupancy of the eight-fold Ca cation site in tremolite impedes the ability of the structure to undergo the chain rotations that break and form the new bonds associated with the symmetry changes of clinoamphiboles with smaller M4 site cations: this scenario appears consistent with our bond-valence calculations.

The persistence of metastable tremolite at low temperatures and/or short times is fully consistent with its behavior under shock loading. Simakov and Trunin (1980) have shown that the shock velocity-particle velocity trend of shocked tremolite is close to linear up to ~65 GPa, implying that tremolite undergoes no major phase transitions at the high pressures, high temperatures, and rapid times of shock-loading up to this pressure. Simakov and Trunin (1980) present two shock data sets on tremolite with different initial sample porosities; the more extensive of these is, in conjunction with the bulk sound velocity of Brown and Abramson (2016), mildly better fit by a concave-upward quadratic. Although their data are sparse, such curvature is consistent with a compression-induced increase in the first derivative of the bulk modulus (e.g., Ruoff, 1967) and associated positive value of  $K''$ , as is observed in Figure 5 under compression. The planetary importance of this observation lies in the demonstration that Ceres-sized, tremolite-rich, hydrated parent asteroidal bodies were present in the early solar system (Hamilton et al., 2021), as well as the inference that tremolite may be abundant in hydrothermally altered basaltic crust on both Mars and Venus (Griffith and Shock, 1995; Johnson and Fegley, 2000, 2003). Thus, our results on the elasticity and metastability of tremolite can provide a direct comparison with Hugoniot results, and are hence relevant to the

properties of tremolite-bearing asteroids and planetary crusts under shock during accretionary events. Metastable tremolite has also been invoked as playing a primary role in both intermediate-depth earthquakes and in generating conductivity anomalies at depths substantially deeper than its equilibrium stability within subduction zones (Scambelluri et al., 2017; Shen et al., 2020). These results mirror recent results on glaucophane, which indicate its persistence at low temperatures to depths (240 km, or  $\sim 8$  GPa) well beyond its formal thermodynamic stability limit ( $\sim 3$  GPa: Cheng et al., 2020) (Bang et al., 2021). Thus, our results strongly indicate that tremolite should be stable in the  $C2/m$  space group throughout its persistence interval within the planet. Moreover, our results demonstrate that the elastic anisotropy of tremolite markedly decreases under compression: hence, calculations of the seismic anisotropy of mineral assemblages within subduction zones that are based on the zero-pressure elastic anisotropy of tremolite could markedly underestimate the amount of tremolite at depth. Our single-crystal results further document that, at 300 K, tremolite in the  $C2/m$  space group has the largest documented range of metastability of any amphibole phase persisting within the same space group, and that this metastability is likely generated by the role of large calcium cations in preventing the chain readjustments that generate phase transitions in other amphiboles.

Finally, we note that the interplay between the calcium ion's presence in tremolite and the inability of the tetrahedral chains to readjust may produce a structural contrepemps that has a likelihood of ultimately generating a structural instability (and possibly amorphization) at 300 K at pressures higher than  $\sim 40$  GPa. As previously noted, tracking of single-crystal diffraction from tremolite proved impossible above this pressure due to the poor peak/background ratio of the diffraction data. This loss of intensity occurred within the quasi-hydrostatic pressure range of the neon pressure-medium, and was accompanied by no visible damage to the tremolite single-

crystal. Similar peak/background ratio degradation has been reported previously at high pressures in  $\alpha$ -quartz by Hazen et al. (1989), where it was interpreted as the initial manifestation of an incipient crystal-amorphous transition in the sample. Our previous Raman results were able to track bands associated with tremolite to  $\sim 49$  GPa (Ott and Williams, 2020), but the high sensitivity of single-crystal X-ray diffraction peaks to mosaic spread in the sample facilitates earlier observation of the onset of sample amorphization (Hazen et al., 1989). This evidence in conjunction with both the marked stiffening of our current elastic results in regime III and the marked decrease in pressure-shifts of most lattice mode shifts of tremolite in the pressure range between 39 and 49 GPa indicate that tremolite may well be approaching a lattice instability, even within a quasi-hydrostatic pressure medium.

Tremolite represents the Mg-rich endmember of the tremolite-actinolite-ferro-actinolite solid solution, and it is thus interesting to consider the effect of increasing amounts of  $\text{Fe}^{2+}$  substitution for  $\text{Mg}^{2+}$  in the M1, M2, and M3 sites of actinolite and ferro-actinolite. Any substitution of high-spin  $\text{Fe}^{2+}$  for  $\text{Mg}^{2+}$  in these octahedral sites results in an increase in the size of the central cation in these units, which may, in turn, induce a structural instability at lower pressures. In an infrared spectroscopic study of the hydroxyl vibrations of amphiboles at high pressures (Thompson et al., 2016), the pressure-shift of the hydroxyl B-band of actinolite (which is associated with a single Fe substitution in the three M1/M3 octahedral sites that coordinate the hydroxyl groups) decreases to a near-zero pressure-dependence above  $\sim 30$  GPa, which is evocative of a saturation of the compression mechanism for this vibration. For comparison, the hydroxyl A-band, which is coordinated by 3 Mg-ions, continues to increase with compression. Hence, the presence of Fe appears to modulate the behavior of the hydroxyl bond in amphiboles above 30 GPa. We speculate that increasing  $\text{Fe}^{2+}$  substitution on the tremolite-ferro-actinolite

join carries with it the prospect of decreased metastability ranges for solid solutions with actinolite and ferro-actinolite, respectively.

Acknowledgments: This work was supported by NSF EAR-2017294, and used resources of the Advanced Light Source (beamline 12.2.2) at Lawrence Berkeley National Laboratory which is a DOE Office of Science User facility under Contract No. DE-AC02-05CH11231. This research was partially supported by COMPRES, the Consortium for Materials Properties Research in Earth Sciences under NSF Cooperative Agreement EAR 1606856. Part of this work was conducted at the Molecular Analysis Facility, a National Nanotechnology Coordinated Infrastructure (NNCI) site at the University of Washington, which is supported in part by funds from the National Science Foundation (awards NNCI-2025489, NNCI-1542101), the Molecular Engineering & Sciences Institute, and the Clean Energy Institute.

## References:

- Angel, R.J. (2000a) High-pressure structural phase transitions. *Reviews in Mineralogy and Geochemistry*, 39, 85–104.
- Angel, R.J. (2000b) Equations of state. *Reviews in Mineralogy and Geochemistry*, 41, 35-57.
- Arlt, T., and Angel, R.J. (2000) Displacive phase transitions in c-centered clinopyroxenes: spodumene,  $\text{LiScSi}_2\text{O}_6$  and  $\text{ZnSiO}_3$ . *Physics and Chemistry of Minerals*, 27, 719-731.
- Arlt, T., Angel, R.J., Miletich, R., Armbruster, T., and Peters, T. (1998) High-pressure  $P2_1/c$ - $C2/c$  phase transitions in clinopyroxenes: influence of cation size and electronic structure. *American Mineralogist*, 83, 1176-1181.
- Bang, H., Hwang, H., Kim, T., Cynn, H., Park, Y., Jung, H., Park, C., Popov, D., Prakapenka, V.B., Wang, L., and others (2021) The stability of subducted glaucophane with the Earth's secular cooling. *Nature Communications*, 12, 1496.
- Bass, J. D. (1995) Elasticity of minerals, glasses, and melts. *Mineral physics and crystallography: A handbook of physical constants*, 2, 45-63.
- Birch, F. (1978) Finite strain isotherm and velocities for single-crystal and polycrystalline NaCl at high pressures and 300°K. *Journal of Geophysical Research: Solid Earth*, 83, 1257–1268.
- Brown, I.D. (2002) *The chemical bond in inorganic chemistry: The valence bond model*. Oxford University Press.
- Brown, J.M., and Abramson, E.H. (2016) Elasticity of calcium and calcium-sodium amphiboles. *Physics of the Earth and Planetary Interiors*, 261, 161-171.
- Bruker (2016) APEX3. Madison, Wisconsin: Bruker AXS Inc. Software.
- Cheng, N., Jenkins, D.M., and Huang, F. (2020) Dehydration of glaucophane in the system

Na<sub>2</sub>O-MgO-Al<sub>2</sub>O<sub>3</sub>-SiO<sub>2</sub>-H<sub>2</sub>O and the effects of NaCl-, CO<sub>2</sub>- and silicate-bearing aqueous fluids. *Journal of Petrology*, 60, 2369-2386.

Comodi, P., Mellini, M., Ungaretti, L., and Zanazzi, P.F. (1991) Compressibility and high-pressure structure refinement of tremolite, pargasite and glaucophane. *European Journal of Mineralogy*, 3(3), 485-499.

Comodi, P., Boffa Ballaran T., Zanazzi, P.F., Capalbo, C., Zanetti, A., and Nazzareni, S. (2010) The effect of oxo-component on the high-pressure behavior of amphiboles. *American Mineralogist*, 95, 1042-1051.

Coppens, P. (1970) The evaluation of absorption and extinction in single crystal structure analysis. In F.R. Ahmed, S.R. Hall, and C.P. Huber, Eds., *Crystallographic Computing*, p. 255-270. Munksgaard, Copenhagen.

Gonzalez-Platas, J., Alvaro, M., Nestola, F., and Angel, R.J. (2016) EosFit7-GUI: A new GUI tool for equation of state calculations, analyses, and teaching. *Journal of Applied Crystallography* 49, 1377-1382.

Griffith, L.L., and Shock, E.L. (1995) A geochemical model for the formation of hydrothermal carbonates on Mars. *Nature* 377, 406-408.

Hamilton, V.E., Goodrich, C.A., Treiman, A.H., Connolly Jr., H.C., Zolensky, M.E., and Shaddad, M.E. (2021) Meteoritic evidence for a Ceres-sized water-bearing carbonaceous chondrite parent asteroid. *Nature Astronomy*, 5, 350-355.

Hawthorne, F.C. (1981) Crystal chemistry of the amphiboles. *Reviews in Mineralogy and Geochemistry*, 9A, 1-102.

Hawthorne, F.C., and Grundy, H.D. (1976) The crystal chemistry of the amphiboles: IV. X-ray and neutron refinements of the crystal structure of tremolite. *The Canadian Mineralogist*,

14, 334-345.

- Hawthorne, F.C., and Oberti, R. (2007) Amphiboles: Crystal chemistry. *Reviews in Mineralogy and Geochemistry*, 67, 1-54.
- Hazen, R.M., Finger, L.W., Hemley, R.J., and Mao, H.K. (1989) High-pressure crystal chemistry and amorphization of  $\alpha$ -quartz. *Solid State Communications*, 72(5), 507-511.
- Johnson, N.M., and Fegley, B. (2000) Water on Venus: New insights from tremolite decomposition. *Icarus*, 146, 301-306.
- Johnson, N.M., and Fegley, B. (2003) Tremolite decomposition on Venus II. Products, kinetics and mechanism. *Icarus*, 164, 317-333.
- Klotz, S., Chervin, J.C., Munsch, P., and Le Marchand, G. (2009) Hydrostatic limits of 11 pressure transmitting media. *Journal of Physics D: Applied Physics*, 42, 075413.
- Konzett, J., and Fei, Y. (2000) Transport and storage of potassium in the Earth's upper mantle and transition zone: An experimental study to 23 GPa in simplified and natural compositions. *Journal of Petrology*, 41, 583-603.
- Koziskova, J., Hahn, F., Richter, J., and Kožíšek, J. (2016) Comparison of different absorption corrections on the model structure of tetrakis ( $\mu_2$ -acetato)-diaqua-di-copper(II). *Acta Chimica Slovaca*, 9(2), 136-140.
- Kunz, M., MacDowell, A.A., Caldwell, W.A., Celestre, R., Domning, E., Duarte, R.M., Gleason, A.E., Glossinger, J.M., Kelez, N.M., Plate, D., and others. (2005) A beamline for high-pressure studies at the Advanced Light Source with a superconducting bending magnet as the source. *Journal of Synchrotron Radiation* 12(5), 650-658.
- Mao, H.K., Xu, J., and Bell, P.M. (1986) Calibration of the ruby pressure gauge to 800 kbar under quasi-hydrostatic conditions. *Journal of Geophysical Research*, 91(B5), 4673-

4676.

- Ott, J., and Williams, Q. (2020) Raman spectroscopic constraints on compression and metastability of the amphibole tremolite at high pressures and temperatures. *Physics and Chemistry of Minerals*, 47, 27.
- Papike, J.J., and Clark, J.R. (1968) The crystal structure and cation distribution of glaucophane. *American Mineralogist*, 53, 1156-1173.
- Papike, J., and Ross, M. (1970) Gedrites-crystal structures and intracrystalline cation distributions. *American Mineralogist*, 55, 1945-1972.
- Parsons, S. (2010) ECLIPSE—Program for masking high-pressure diffraction images and conversion between CCD image formats. Software
- Pawley, A.R., and Holloway, J.R. (1993) Water sources for subduction zone volcanism: New experimental constraints. *Science*, 260, 664-667.
- Peng, Y., and Mookherjee, M. (2020) Thermoelasticity of tremolite amphibole: Geophysical implications, *American Mineralogist*, 105, 904-916.
- Poli, S., and Schmidt, M.W. (1995) H<sub>2</sub>O transport and release in subduction zones: Experimental constraints on basaltic and andesitic systems. *Journal of Geophysical Research*, 100, 22299-22314.
- Poli, S., and Schmidt, M.W. (2002) Petrology of subducted slabs. *Annual Review of Earth and Planetary Sciences*, 30, 207-235.
- Prewitt, C.T., Papike, J.J., and Ross, M. (1970) Cummingtonite: A reversible, nonquenchable transition from P2<sub>1</sub>/m to C2/m symmetry. *Earth and Planetary Science Letters*, 8, 448-450.
- Ruoff, A.L. (1967) Linear shock-velocity-particle-velocity relationship. *Journal of Applied*

Physics, 38, 4976-4970.

Scambelluri, M., Pennacchioni, G., Gilio, M., Bestmann, M., Plumper, O., and Nestola, F. (2017)

Fossil intermediate-depth earthquakes in subducting slabs linked to differential stress release. *Nature Geoscience*, 10, 960-966.

Schmidt, M.W., and Poli, S. (1998) Experimentally based water budget for dehydrating slabs and

consequences for arc magma generation. *Earth and Planetary Science Letters*, 163, 361-379.

Sheldrick, G.M. (2008) A short history of SHELX. *Acta Crystallographica*, A64, 112-122.

Shen, K., Wang, D., Liu, T. (2020) Electrical conductivity of tremolite under high temperature

and pressure: Implications for the high-conductivity anomalies in the Earth and Venus. *Contributions to Mineralogy and Petrology*, 175, 52.

Simakov, G.V. and Trunin, R.F. (1980) The compressibility of minerals by shock waves.

*Izvestiya Earth Physics*, 16, 134-137.

Stern, R.J. (2002) Subduction zones. *Reviews of Geophysics*, 40(4), 1-38.

Stoe, Cie (2009) X-Area V1.76 Software. Stoe & Cie GmbH, Darmstadt, Germany. Software.

Sueno, S., Papike, J.J., Prewitt, C.T., and Brown, G.E. (1972) Crystal chemistry of high

cummingtonite. *Journal of Geophysical Research*, 77, 5767-5777.

Sueno, S., Cameron, M., Papike, J.J., and Prewitt, C.T. (1973) The high temperature crystal

chemistry of tremolite. *American Mineralogist*, 58, 649-664.

Thompson, E.C., Campbell, A.J., Liu, Z. (2016) In-situ infrared spectroscopic studies of

hydroxyl in amphiboles at high pressure. *American Mineralogist*, 101, 706-712.

Tribaudino, M., Prencipe, M., Nestola, F., and Hanfland, M. (2001) A  $P2_1/c-C2/c$  high-

pressure phase transition in  $\text{Ca}_{0.5}\text{Mg}_{1.5}\text{Si}_2\text{O}_6$  clinopyroxene. *American Mineralogist*,

86, 807-813.

Whittaker, E.J.W. (1960) The crystal chemistry of the amphiboles. *Acta Crystallographica*, A13, 291-298.

Wong-Ng, W., Siegrist, T., DeTitta, G. T., Finger, L. W., Evans, H. T. Jr., Gabe, E. J., Enright, G.D., Armstrong, J.T., Levenson, M., Cook, L.P. and Hubbard, C.R. (2001) Standard Reference Material (SRM 1990) for single crystal diffractometer alignment. *Journal of Research of the National Institute of Standards and Technology*, 106(6), 1071–1094.

Yang, H., and Evans, B.W. (1996) X-ray structure refinements of tremolite at 140 and 295 K: chemistry and petrological implications. *American Mineralogist*, 81, 1117-1125.

Yang, H., Hazen, R.M., Prewitt, C.T., Finger, L.W., Lu, R., and Hemley, R.J. (1998) High-pressure single-crystal X-ray diffraction and infrared spectroscopic studies of the  $C2/m$ - $P2_1/m$  phase transition in cummingtonite. *American Mineralogist*, 83, 288-299.

Yang, H., and Prewitt, C.T. (2000) Chain and layer silicates at high temperatures and pressures. *Reviews in Mineralogy and Geochemistry*, 41, 211-255.

Yang, H., and Smyth, J.V. (1996) Crystal structure of  $P2_1/m$  ferromagnesian cummingtonite at 140 K. *American Mineralogist*, 81, 363-368.

Yong, T., Dera, P., and Zhang, D. (2019) Single-crystal X-ray diffraction of grunerite up to 25.6 GPa: a new high-pressure clinoamphibole polymorph. *Physics and Chemistry of Minerals*, 46, 215-227.

Figure 1: Ambient pressure structure of the amphibole mineral tremolite, crystallizing in the  $C2/m$  space group. Hydroxyl units, extending from O3 into the cavity in the ring of  $\text{SiO}_4$  tetrahedra were not resolved in the XRD data, and are not displayed in the structure.

Figure 2: The normalized unit cell parameters ( $a/a_0$ ,  $b/b_0$ , and  $c/c_0$ ) and the normalized volume ( $V/V_0$ ) of tremolite to  $\sim 39$  GPa. Set 0 (gray markers) at ambient conditions, Sets 1, 2, and 3 at high pressures in DAC with Ne pressure-medium. Uncertainties of the parameters are contained within the markers. The deviation of set 3 from the other results above 22 GPa might be associated with the onset of undetected non-hydrostatic conditions in the sample (e.g., possible bridging of the crystal).

Figure 3: Response of the  $\beta$ -angle of  $C2/m$  monoclinic space-group member tremolite to high pressures in Ne pressure-transmission medium loaded DAC. Uncertainties are contained within the markers.

Figure 4: Unit cell parameter ratios **a**  $a/b$  and **b**  $a/c$  for the monoclinic amphiboles tremolite with increasing pressure. Plots of the ratios for cummingtonite (Yang et al., 1998), and grunerite (Yong et al., 2019) included for comparison. Slopes of the axial ratios for each region are fit linearly by least squares.

Figure 5: **a**  $F_E-f_E$  plot for tremolite with least squares fit lines for the determination of  $K_{0T}$  and  $K'_{0T}$  for each compression-regime and **b** the unit cell volumes of tremolite plotted with fits of a third-order Birch-Murnaghan (B-M) equation of state. Chi-squared test results of EoS fit are 0.09

(regime I), 0.14 (regime II), and 0.96 (regime III). A larger Chi-squared value in regime III is anticipated, given the scatter in this portion of the dataset and the extrapolation to  $V_0$  at ambient pressure from a small dataset at these high pressures. Nevertheless, the fit values for  $V_0$  in each regime were essentially indistinguishable from the observed ambient pressure value. Dotted black curve is 3<sup>rd</sup> order B-M fit to regime I with constrained  $K_0$  value of 78 GPa (after Brown and Abramson, 2016). **c** Confidence ellipses at the 68.3% level in  $K_0$  and  $K'$  for the 3<sup>rd</sup> order equation of state fits in regime I, II, and III. Confidence ellipses at the 99.9% level extend to non-physical (negative)  $K_0$  values and are not included. **d** Volume-pressure data fit with a fourth-order B-M equation of state. Chi-squared test of EoS fit is 0.33, and this fit yields an unusual  $K'$  value of 0.221. **e** 68.3% and 99.9% confidence ellipses in  $K_0$  and  $K'$  for the 4<sup>th</sup> order B-M EoS fit display much smaller  $K'/K_0$  spread than our 3<sup>rd</sup> order B-M results due to the addition of a refinable  $K''$  parameter.

Figure 6: **a-f** Refined bond lengths within different polyhedra in tremolite. Datasets 1 and 2 did not yield stable structural refinements, therefore only set 3 (supplemental table S2) is shown. Lines are trends within each compressional regime that are noted in the text and are intended solely to guide the eye.

Figure 7: **a** Bond angles associated with tetrahedral chains in tremolite. Tetrahedral rotation angles calculated as average deviation of six-member ring-associated O-O-O angles (unfilled symbols) from 120°. **b** Polyhedral volumes as a function of compression. **c** I-beam thicknesses and spacing under pressure; O4 separations correspond to the edge of the I-beam, and O7 distances correspond to its center. **d-f** Tremolite structural evolution with increasing pressure

viewed normal to the *b-c* plane displays modification of SiO<sub>4</sub> tetrahedra into an increasingly O-rotated configuration. Tetrahedra are O-rotated by 12.5° at ambient conditions, **d** 15.6° at 4.24 GPa, **e** 21.9° at 13.1 GPa, and **f** 28.7° at 29.2 GPa. Both silica double-chains are symmetrically equivalent as the tremolite structure retains *C2/m* symmetry throughout this study. Datasets 1 and 2 did not yield stable structural refinements, therefore only set 3 (supplemental table S2) is shown. Arrows have been added to panels **e** and **f** to illustrate the relative motion of corner-shared oxygens resulting from the rotation of silica tetrahedra.

Figure 8: Normalized cation overbonding versus pressure for tremolite, calculated as (bond-valence sum – cation charge)/cation charge. Uncertainties are calculated from an order-of-magnitude estimate of bond length uncertainty propagated through the overbonding calculation for a maximum uncertainty of ±3.5%. Datasets 1 and 2 did not yield stable structural refinements, therefore only set 3 (supplemental table S2) is shown.

Table 1: Ambient conditions single-crystal structure refinement for  $C2/m$  tremolite.

Atom	x	y	z	$U_{eq}$
Mg1	0	0.08798(10)	0.5	0.0054(4)
Mg2	0	0.17640(10)	0	0.0051(4)
Mg3	0	0	0	0.0047(5)
Ca1	0	0.27794(6)	0.5	0.0085(3)
Si1	0.28088(9)	0.08394(5)	0.29756(19)	0.0046(3)
Si2	0.28861(8)	0.17115(6)	0.80553(19)	0.0042(3)
O1	0.1121(2)	0.08555(14)	0.2182(5)	0.0058(6)
O2	0.1188(2)	0.17053(15)	0.7242(5)	0.0061(6)
O3/F <sup>a</sup>	0.1064(3)	0	0.7145(6)	0.0091(12)
O4	0.3651(2)	0.24807(15)	0.7924(5)	0.0068(6)
O5	0.3465(2)	0.13441(15)	0.1000(5)	0.0065(6)
O6	0.3445(2)	0.11887(15)	0.5895(5)	0.0065(6)
O7	0.3385(3)	0	0.2932(7)	0.0076(8)
Measured reflections			3421	
Independent reflections			845	
Parameters refined			97	
$R_{int}$			0.0969	
Goodness of fit			1.054	
$wR_2$			0.0991	
$R_I$ (all 845 data)			0.0523	
$R_I$ (677 data $F_o > 4 \sigma_{F_o}$ )			0.0378	

a: Substitutional disorder of O3/F refined to 0.56(7)/0.44(7) occupancy

Table 2: Unit cell parameters and volumes of tremolite at pressures up to 38.7 GPa.

Set	Pressure (GPa)	a (Å)	b (Å)	c (Å)	$\beta$ (°)	V (Å <sup>3</sup> )
0	0.0001	9.833(2)	18.046(4)	5.274(1)	104.76(3)	904.9(3)
1	1.0	9.751(7)	17.9836(10)	5.2613(3)	104.923(20)	891.5(7)
2	1.9	9.707(2)	17.9663(13)	5.2485(3)	104.949(8)	884.4(2)
1	2.5	9.675(8)	17.9115(12)	5.2423(4)	105.210(20)	876.7(7)
1	3.7	9.598(6)	17.8530(8)	5.2253(2)	105.183(17)	864.1(5)
3	4.2	9.6198(55)	17.8738(100)	5.2280(28)	105.192(11)	867.5(8)
1	4.9	9.558(4)	17.7960(11)	5.2106(3)	105.276(13)	854.9(4)
2	5.9	9.519(2)	17.7856(13)	5.2010(3)	105.185(9)	849.8(2)
1	7.2	9.476(4)	17.6935(10)	5.1863(3)	105.397(13)	838.3(3)
1	8.8	9.423(4)	17.6235(11)	5.1690(3)	105.455(14)	827.4(4)
2	9.4	9.407(2)	17.6438(14)	5.1681(3)	105.284(9)	827.4(2)
3	9.6	9.4132(5)	17.614(9)	5.163(3)	105.374(11)	825.4(8)
2	10.0	9.392(3)	17.6175(15)	5.1618(3)	105.287(9)	823.9(2)
1	10.3	9.383(4)	17.5682(10)	5.1548(3)	105.469(13)	818.9(3)
1	11.1	9.335(4)	17.5408(10)	5.1489(3)	105.485(13)	812.5(4)
2	11.6	9.334(2)	17.5575(14)	5.1483(3)	105.272(9)	813.9(2)
1	12.0	9.305(3)	17.5050(9)	5.1402(2)	105.523(11)	806.7(3)
1	12.9	9.289(4)	17.4767(10)	5.1332(3)	105.525(12)	803.0(3)
3	13.1	9.2896(49)	17.4387(84)	5.1176(26)	105.404(11)	799.3(7)
2	13.9	9.268(2)	17.4762(14)	5.1305(3)	105.274(9)	801.6(2)
1	14.3	9.245(4)	17.4204(10)	5.1190(3)	105.499(12)	794.4(3)
2	14.8	9.233(2)	17.4362(14)	5.1217(3)	105.247(9)	795.5(2)
1	15.3	9.228(4)	17.3850(10)	5.1133(3)	105.476(12)	790.6(3)
1	16.2	9.202(4)	17.3576(11)	5.1049(3)	105.454(14)	785.9(3)
3	16.8	9.2335(66)	17.3323(118)	5.0946(36)	105.395(11)	786.1(10)

1	17.4	9.170(5)	17.3214(12)	5.0983(3)	105.388(15)	780.8(4)
2	22.1	9.040(3)	17.1989(16)	5.0800(3)	105.119(11)	762.5(2)
3	23.6	9.0287(100)	16.9959(182)	5.0135(55)	105.305(15)	742.0(14)
2	24.5	8.994(3)	17.1392(18)	5.0696(3)	105.153(11)	754.3(2)
2	28.0	8.920(4)	17.0400(30)	5.0555(5)	105.000(17)	742.2(3)
3	29.2	8.8076(104)	16.7122(166)	4.9411(49)	105.067(23)	702.3(13)
2	31.3	8.894(5)	17.0140(30)	5.0460(5)	105.192(16)	736.9(3)
2	33.1	8.870(5)	16.9630(30)	5.0404(5)	105.217(18)	731.8(4)
2	35.8	8.846(7)	16.9510(40)	5.0334(7)	105.310(20)	727.9(5)
2	38.7	8.749(8)	16.8430(50)	5.0211(7)	105.130(20)	714.3(6)

---

Note: Tremolite structure symmetry is  $C2/m$  for all pressures investigated. Set 0 is the ambient conditions dataset, sets 1, 2, and 3 are high-pressure DAC measurements in a Ne gas transmission medium. Structural refinements were unstable for sets 1 and 2, therefore high-pressure structural refinements have only been reported for set 3 (supplemental table S2).

Table 3: Third-order Birch-Murnaghan equation of state fit data for tremolite.

Compression				
Regime	I	I <sup>a</sup>	II	III
$P_{\min}$ (GPa)	0.0001	0.0001	7.2	22.1
$P_{\max}$ (GPa)	5.9	5.9	17.4	38.7
$K_{0T}$ (GPa)	72(7)	78 <sup>a</sup>	77(2)	61(1)
$K'_{0T}$	8.6(42)	5.7(21)	6.0(3)	10.0(2)
$V_0$	904.48(328)	904.15(181)	905.03(146)	902.51(123)
$\beta_a$	0.0082(4)		0.0053(17)	0.0029(10)
$\beta_b$	0.0037(19)		0.0025(8)	0.0028(4)
$\beta_c$	0.0029(2)		0.0024(13)	0.0021(1)
$\beta_a:\beta_b:\beta_c$	2.22:1.0:0.78		2.12:1.0:0.96	1.03:1.0:0.75

a: Constrained fit with a fixed bulk modulus of 78 GPa

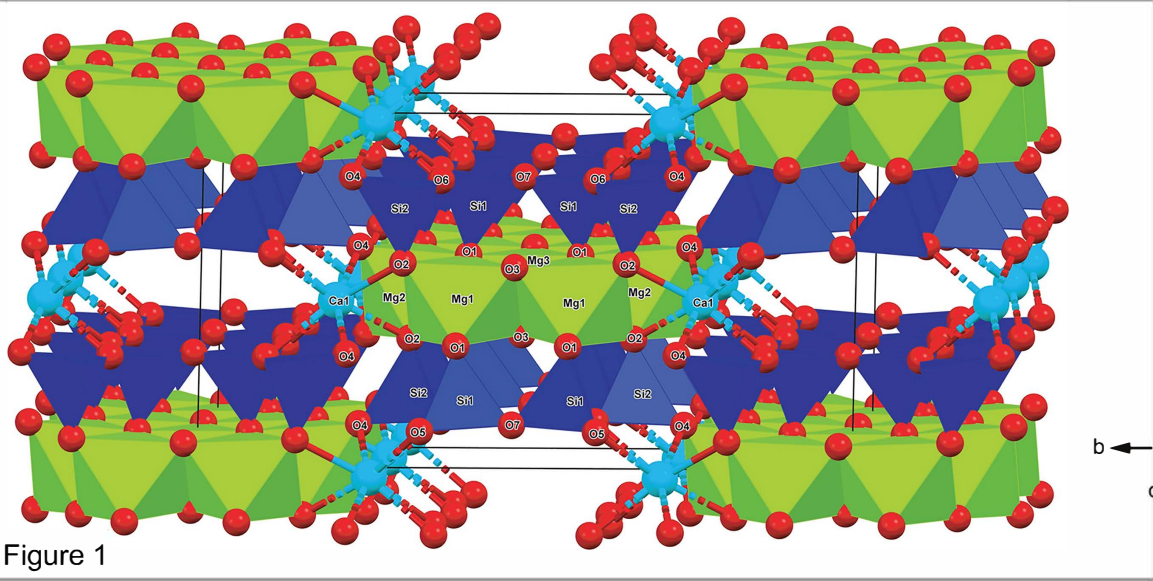


Figure 1

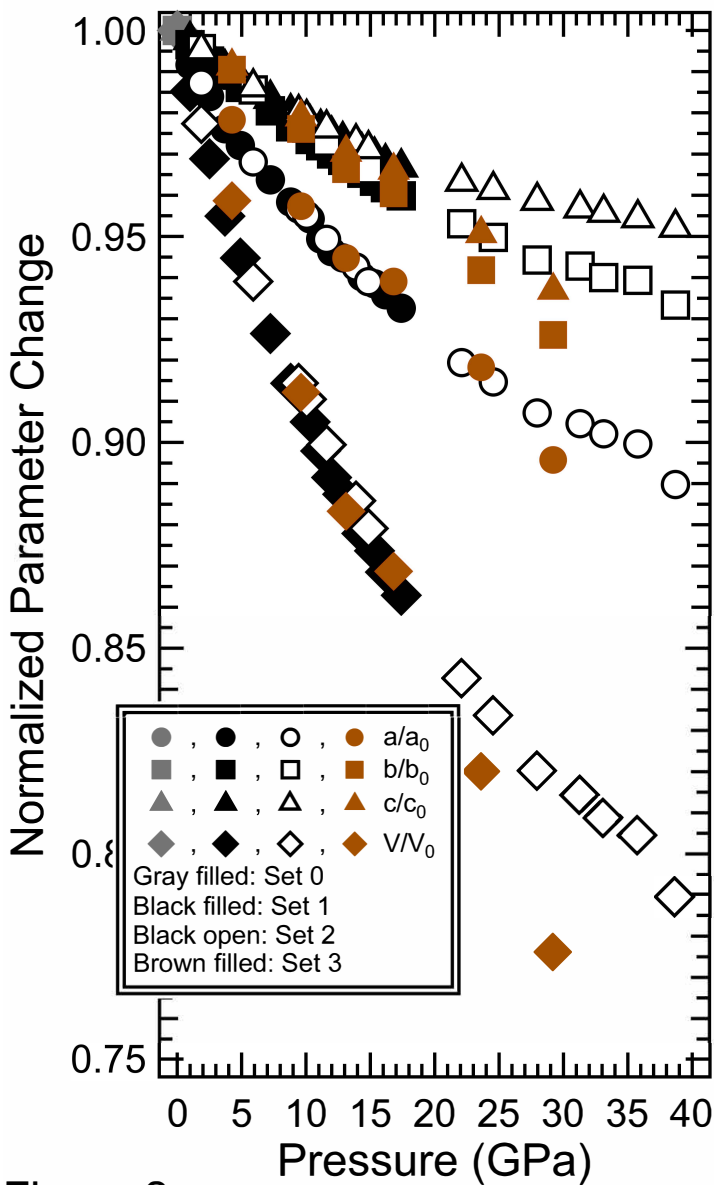


Figure 2

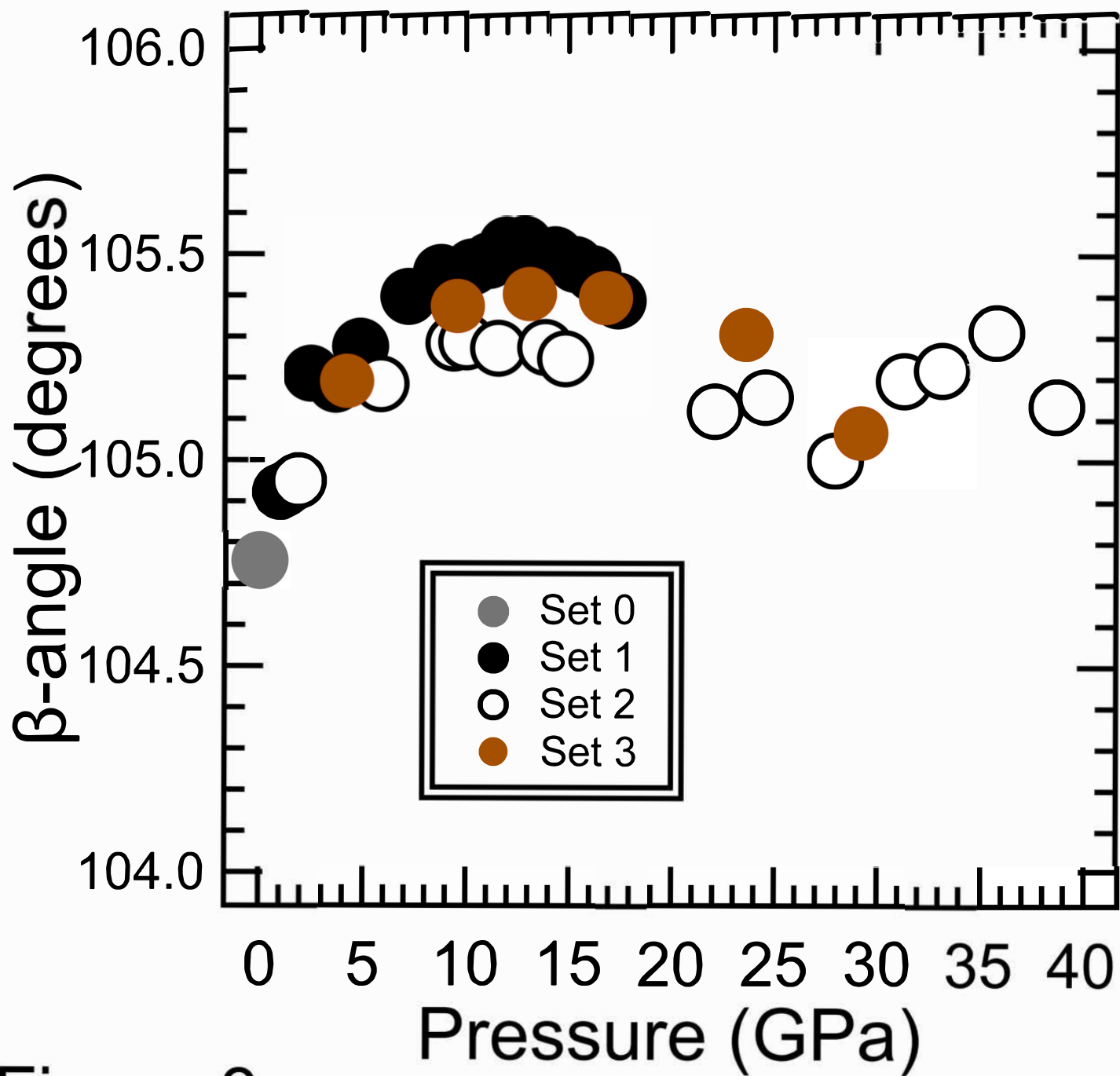


Figure 3

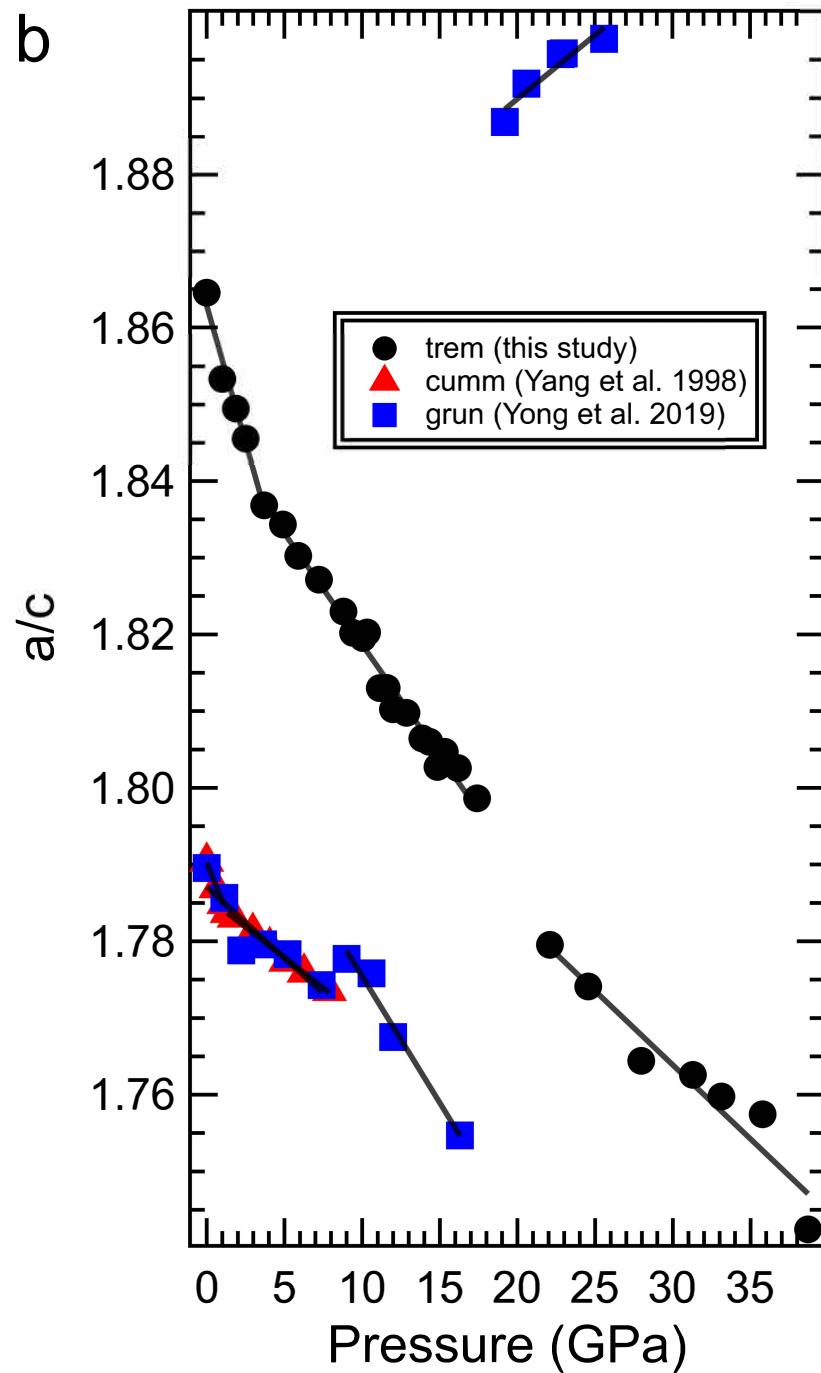
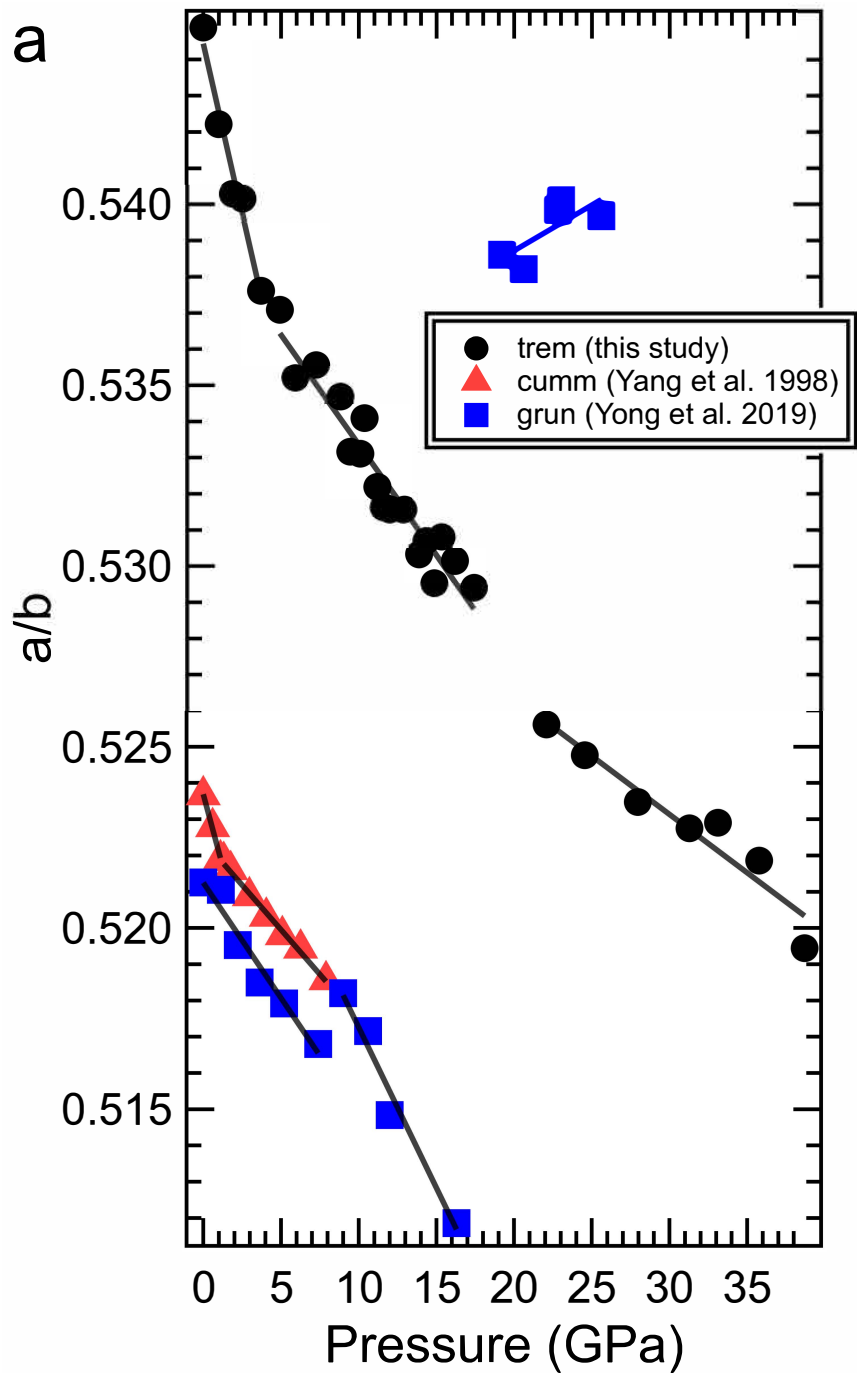


Figure 4

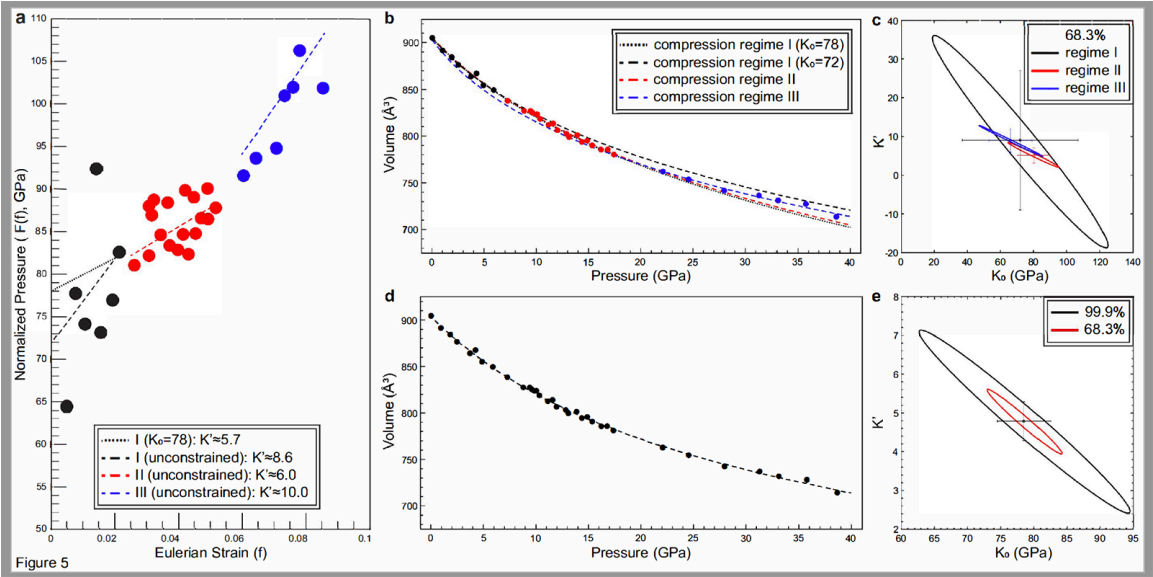


Figure 5

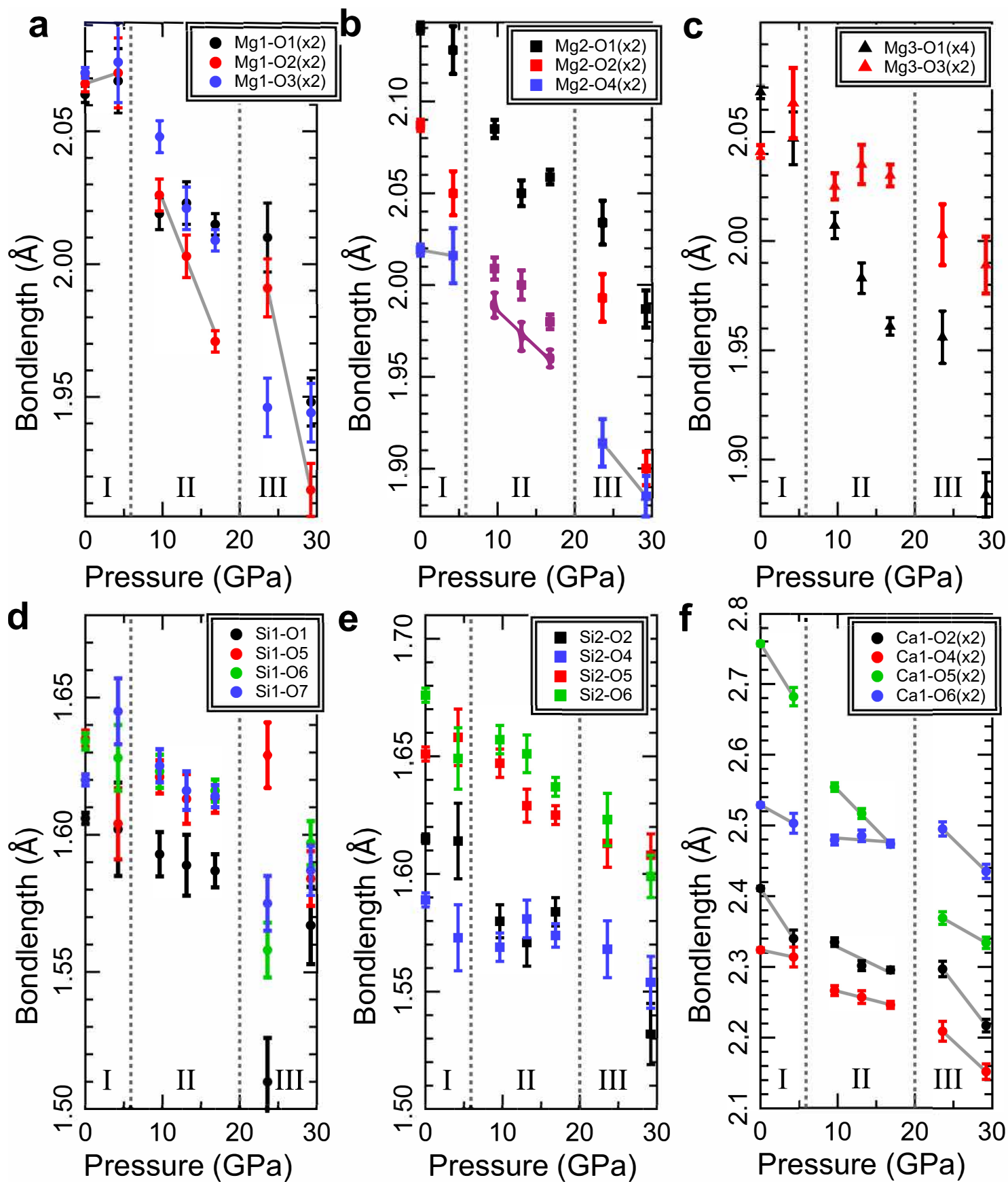


Figure 6

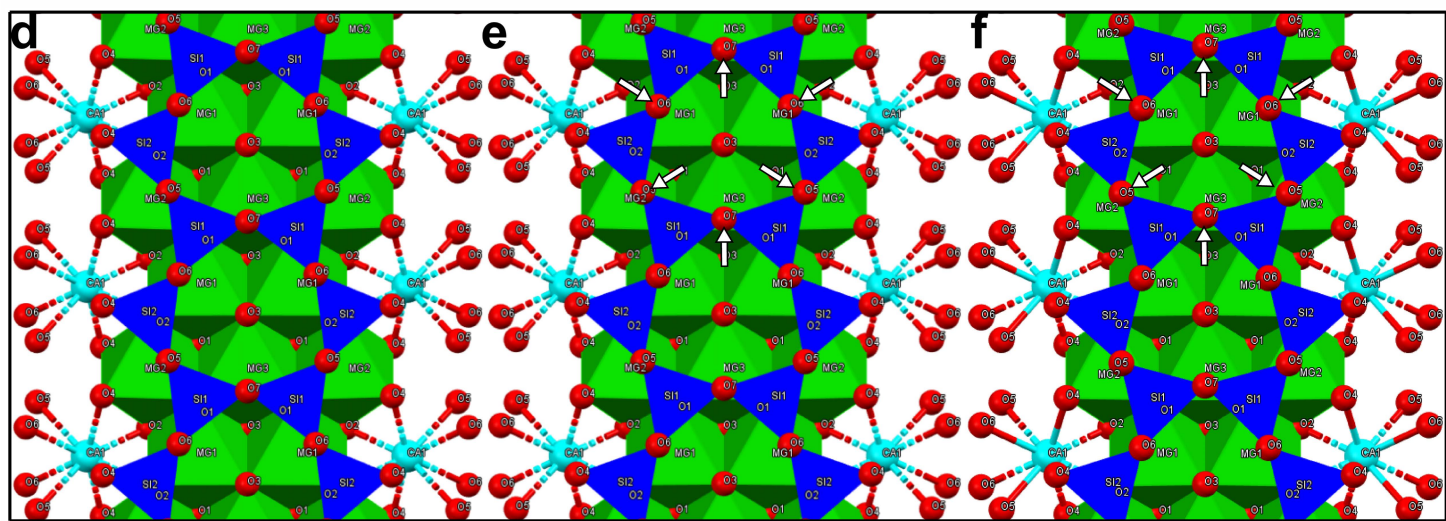
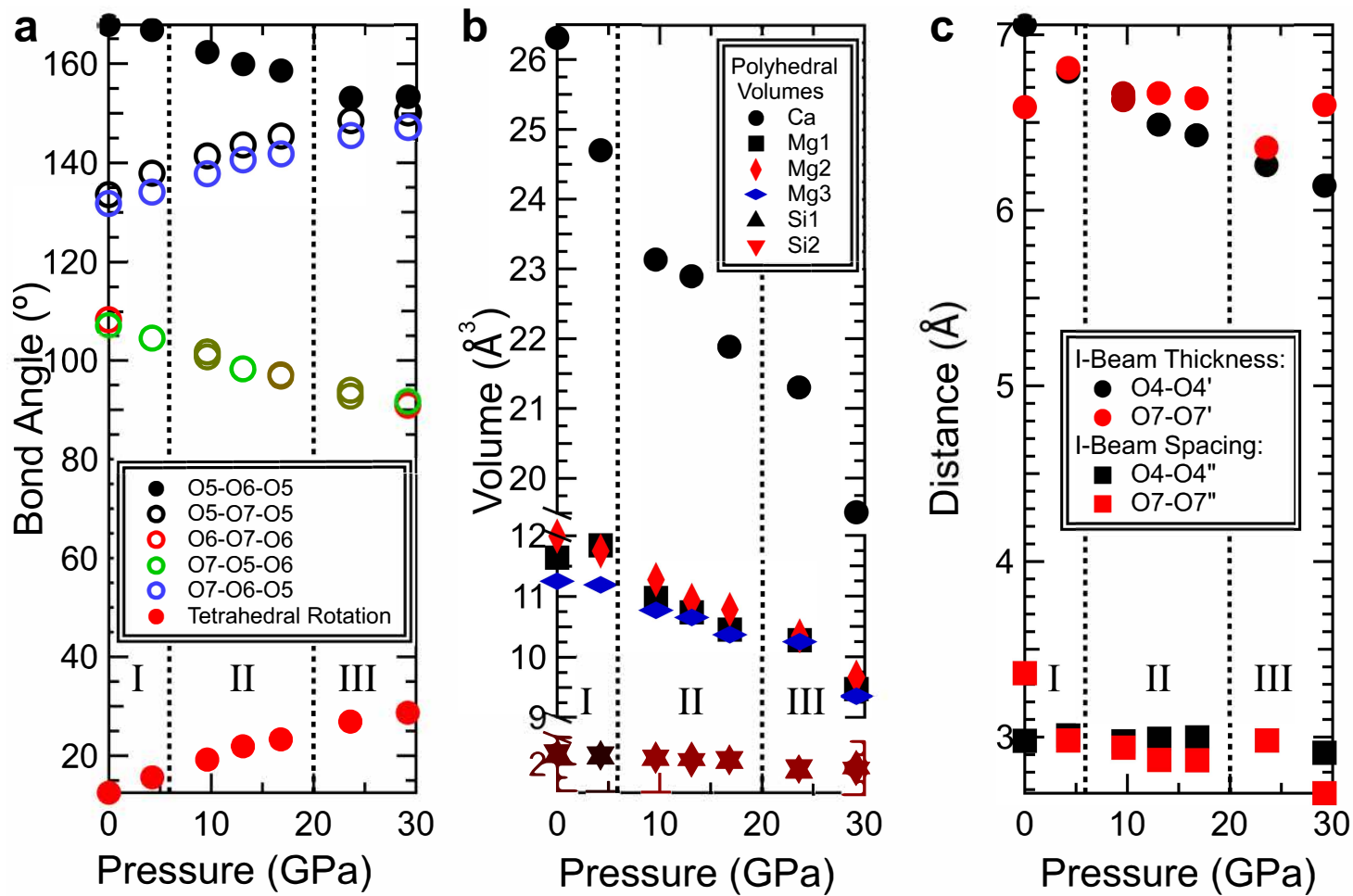


Figure 7

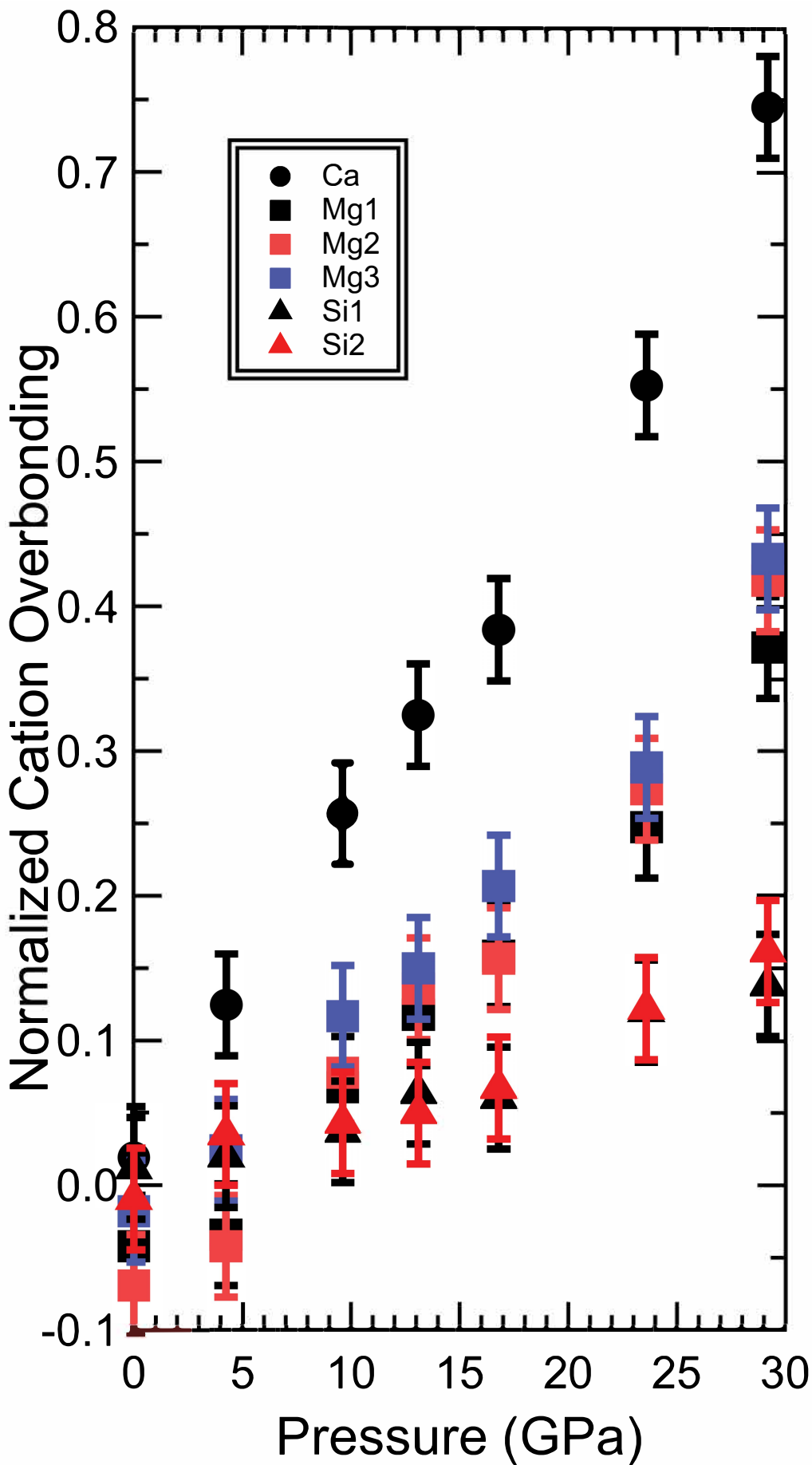


Figure 8